Hindawi
Advances in Civil Engineering
Volume 2024, Article ID 8307250, 13 pages
https://doi.org/10.1155/2024/8307250

Research Article

Research on the Application of Prefabricated Load-Bearing Structure in Prefabricated Roadway in Filling Body

Ke Jiang,[1,2,3] **Gaofeng Ren**,[1] **Jia Sheng**,[2,3,4] **Liang Peng**,[2,3] **Hao Zhu**,[2,3] **Xinyu Tan**,[1,2,3] **Bokun Zheng**,[2,3] **and Congrui Zhang**[1]

[1]*School of Resources and Environmental Engineering, Wuhan University of Technology, Wuhan, Hubei 430070, China*
[2]*Changsha Mining Research Institute Co. Ltd., Changsha, Hunan 410012, China*
[3]*State Key Laboratory of Safety Technology for Metal Mines, Changsha, Hunan 410012, China*
[4]*School of Resources Environment and Safety Engineering, Hunan University of Science and Technology, Xiangtan 411201, China*

Correspondence should be addressed to Gaofeng Ren; rgfwhut@163.com

Received 27 December 2023; Revised 19 March 2024; Accepted 30 March 2024; Published 20 April 2024

Academic Editor: Tingting Zhang

The re-excavation roadway in the filling body is a common engineering demand in mines. In order to solve the problem of instability and failure of the filling body caused by the excavation disturbance in the filling body and improve the comprehensive economic benefits of the technology, it is proposed to use the filling body formed by membrane bag filling in the goaf and the steel arch frame to form a prefabricated load-bearing structure, reserve the required roadway space, avoid the safety risks caused by roadway excavation, and reduce the difficulty and cost of roadway support in the later stage. Based on the background of a mine goaf, the mechanical model of the load-bearing structure is established, and the analytical solution of the bearing capacity of the steel arch is obtained. The optimal ratio of the membrane bag filling of the load-bearing structure is obtained by indoor test, and the deformation of the surrounding rock and the distribution range of the plastic zone after the formation of the reserved roadway are numerically simulated and analyzed. The results show that the best cementing material is cement : fly ash of 8 : 2, and the ratio of cement to sand is 1 : 3. The vertical displacement of the roof is 45.1 mm, the vertical displacement of the floor is 5.1 mm, and the horizontal displacement of the left side is 55.5 mm. The load on the load-bearing structure is within the allowable range, and the field monitoring results show that the deformation of the reserved roadway is small. The research results can provide reference for the prefabricated roadway engineering in the filling body.

1. Introduction

The exploitation of metal mine resources is very important to promote economic development and meet the growing industrial demand. However, with the gradual depletion of near-ground resources and the increasingly prominent environmental and safety issues, efficient and environmentally friendly metal mine resource mining has become one of the current research hotspots [1–4]. A large number of studies have shown that the filling method can effectively maintain the stability of the surrounding rock and improve the stress environment of the surrounding rock, so as to ensure the safety of the working face and the long-term sustainable mining of the mine. Therefore, it is widely used in metal mines. In order to recover the pillar in the subsequent filling, so as to realize the efficient recovery of resources, it is necessary to re-excavate the roadway in the filling body. Drilling and blasting method or cantilever roadheader is often used to re-excavate the roadway in the filling body. Because the filling body has the characteristics of low strength, strong plasticity, and poor stability compared with the rock, it is necessary to support in advance to ensure the stability of the filling body during excavation. In this regard, many scholars at home and abroad have carried out in-depth research on the stability of filling roadway [5–7]. He and Wang [8] believed that all kinds of excavation disturbances have a significant impact on the stability of the roadway. Based on the engineering practice, Ke [9] took the excavation roadway in the filling body of a mine as the research background. Through the discussion and analysis of the process scheme, excavation efficiency and cost, through technical and economic

comparison, the most suitable combined support scheme and excavation method for the excavation roadway of the mine were finally obtained. Luo [10] established a 3D numerical model for dynamic stability analysis of roadway by using 3DEC numerical simulation technology, and studied the stability of reserved roadway in filling body under blasting disturbance. Deng et al. [11] used numerical simulation technology to study the failure law and dynamic response law of filling body under different disturbance amplitudes and found that dynamic disturbance had a significant effect on the vibration characteristics of filling body. In nonmetallic mines, gob-side entry retaining has been widely used. Through effective support technology, the mining roadway is retained, thereby reducing the roadway excavation rate [12].

In order to avoid the unfavorable factors of roadway excavation in filling weight, based on the existing research results and practical experience, the roadway formation method of reserved roadway in goaf is proposed. By setting up steel support and filling membrane bag in the prefilling area, the load-bearing structure of reserved roadway is formed, and the roadway can be formed after filling the empty area. Taking the filling of a mine as the engineering background, the author studies the reserved roadway in the filling body through mechanical analysis, indoor test, and numerical simulation, and determines the reasonable reserved roadway scheme, which provides reference for similar engineering cases.

2. Engineering Background

2.1. Geological Overview of the Goaf Area. The mining operation in the +650 m midsection 4001# stope of a specific mine employs a sublevel rock drilling followed by filling method. Following the complete recovery of the stope, there arises a necessity to extract the ore pillar and address the transportation needs of the overlying mining area. Consequently, a transportation roadway needs to be established within the filling body of the 4001# stope. Geological data indicate that the predominant rocks in the roof, floor, and interlayer of this stope are sericite graphite schist, followed by dolomite marble and graphite–dolomite marble. The stope is situated in a fractured zone due to geological structures. The mining range spans from +650 m to + 700 m, resulting in a goaf measuring 58.8 m in length, 15 m in width, and 44 m in height, with a volume of approximately 3.88×104 m³, following mining activities. In situ stress measurement results indicate a vertical stress of 15.1 MPa in the stope, with a lateral pressure coefficient of 1. The filling procedures involve a mixture of whole tailings, PO 42.5 cement, and fly ash in specific proportions to create the filling slurry. The designed cross-section of the roadway within the filling body is horseshoe shaped, with a roadway cross-section size of $4 \times 3\ m^2$.

2.2. Scheme for Reserved Roadway in the Filling Body. Within the 4001# stope, a reserved roadway is crafted using steel arches with a height and width of 4 m × 3 m. Constructed from Grade 36 U-shaped steel, these arches are spaced at 0.8-m intervals. To enhance overall load-bearing capacity, reinforcing bars, comprising HRB500 left-handed ribbed bars without longitudinal ribs, are evenly placed on the top and sides of the steel arches. The entire support structure is anchored to the floor rock. Filling membrane bags are positioned on the outer side of the support structure and aligned along the outer edge of the steel arches. Through compressed air grouting, a filling slurry with a high cement-to-sand ratio is injected into the bags, creating a filling body with the same shape as the steel arches and a thickness of 1 m. Supported by the steel arches, the slurry in the bags solidifies into a filling body with specific strength, collectively forming the high-strength load-bearing structure required for the reserved roadway. After completing the support for the reserved roadway, the entire goaf is sealed, and the filling slurry injection into the goaf is carried out in three stages. The first stage has a filling height of 8 m. To prevent excessive self-weight pressure from the filling slurry that might damage the load-bearing structure, the second-stage filling takes place after the final setting of the first-stage filling body. The height of the second-stage filling body is 34 m. The third stage involves filling the upper part of the goaf, with a filling height of 2 m. The schematic representation of the reserved roadway formation in the filling body is depicted in Figure 1. After the roadway is formed, a protective layer, 80 mm thick, is sprayed onto the inner wall using C20 concrete. This not only upholds the stability of the roadway but also protects the steel arches from oxidation.

3. Filling Body Mechanical Performance Testing

3.1. Preparation and Test Scheme for Filling Body. The filling slurry is conveyed from the surface filling station through pipelines to the goaf. Subsequently, through a natural curing process, it consolidates into a filling body with a specific strength. The strength of this filling body primarily depends on the concentration and cement-to-sand ratio of the filling slurry, which represents the proportions of aggregates, cementitious materials, and water. The test materials include whole tailings, PO 42.5 Portland cement, and fly ash. The slurry is uniformly poured into standard triple molds, each measuring 7.07 cm × 7.07 cm × 7.07 cm. The filling and scraping procedures of the molds are executed based on the settling and solidification conditions of the slurry. After a designated period of 24 hr, the demolding process ensues, with a subsequent examination of the specimens for adherence to flatness standards. Any specimens failing to meet the standards undergo a repreparation process. For those specimens meeting the stipulated standards, they embark on the standard curing journey, subject to prescribed conditions [13]. Uniaxial compressive strength tests are conducted at intervals of 3, 7, and 28 days. A detailed test plan is outlined in Table 1.

The experimental setup employs the RYL-600 triaxial rock shear rheometer, as illustrated in Figure 2. This equipment consists of the mainframe, hydraulic source, servo control system, and data collection system. It is capable of conducting single-axis, double-axis, and three-axis compression tests, as well as rock shear and rock creep tests. The computer data collection system automatically records test data.

Following the curing process, the uniaxial compression test is conducted through the following steps:

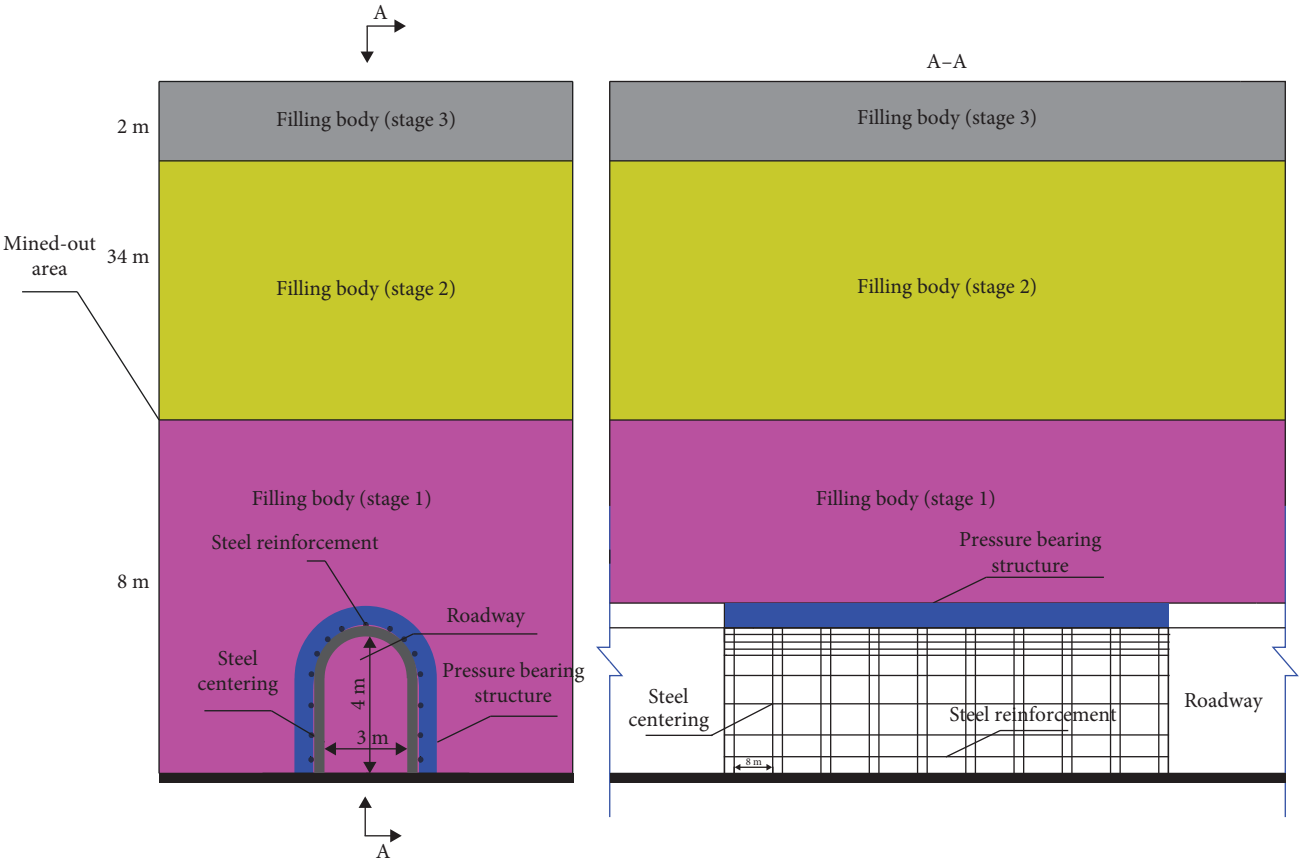

Figure 1: Design layout for the reserved roadway in filling body.

Table 1: Strength ratio test scheme.

Cementitious material	Concentration (%)	Cement-to-sand ratio
Cement	70	1 : 3, 1 : 4, 1 : 6, 1 : 8, 1 : 10
Cement : fly ash = 8 : 2	70	1 : 3, 1 : 4, 1 : 6, 1 : 8, 1 : 10
Cement : fly ash = 7 : 3	70	1 : 3, 1 : 4, 1 : 6, 1 : 8, 1 : 10
Cement : fly ash = 6 : 4	70	1 : 3, 1 : 4, 1 : 6, 1 : 8, 1 : 10

(1) Sand the upper and lower surfaces of the specimen using sandpaper to achieve smoothness.
(2) Apply lubricating oil to the upper and lower surfaces of the specimen and place it on the instrument, awaiting the commencement of the compression test.
(3) Preload the specimen; the test begins when the axial stress reaches 500 N.
(4) Employ the displacement loading mode with a loading rate of 0.3 mm/min until the specimen fails.
(5) Record the specimen's failure and process the data recorded by the computer.

3.2. Analysis of Strength Test Results. The filling body specimens, featuring different ratios listed in Table 1, undergo uniaxial compression tests using the RYL-600 triaxial rock shear rheometer. The resulting uniaxial compressive strength of the filling body under various conditions is measured, and the acquired test data are imported into the origin data analysis software to generate strength curves for the filling body under different ratios, as illustrated in Figure 3. In comparison to rocks, the filling body exhibits relatively low strength under uniaxial compression. The 28-day cured cement-filling body specimen demonstrates the maximum compressive strength, reaching 5.11 MPa. Across all specimens with varying ratios of cementitious materials, a synchronous decline in compressive strength is observed as the cement-to-sand ratio gradually decreases. This phenomenon is attributed to the main components of cementitious materials—tricalcium silicate and dicalcium silicate—reacting with water to yield stable hydrated calcium silicate gel. The lower the content of cementitious materials, the lower the ultimate compressive strength. In specimens where cement and fly ash are mixed in an 8 : 2 ratio, varying compositions of cementitious materials reveal lower compressive strength in the 28-day cured specimens compared to those

Figure 2: RYL-600 triaxial rock shear rheometer.

with pure cement under the same cement-to-sand ratio. However, these mixed specimens outperform pure cement specimens in terms of compressive strength at 3 and 7 days. This discrepancy is attributed to the potential cementitious activity of fly ash, coupled with its finer particle size compared to that of cement and tailings. The smaller particle size of fly ash enables it to effectively fill the gaps between filling aggregates. This, in turn, facilitates the creation of a uniformly structured filling body, enhances slurry workability, and ultimately improves the compactness and compressive strength of the filling body. Furthermore, the fine particles in fly ash possess a larger specific surface area, offering more active surfaces during the cement hydration process. This actively contributes to the generation of hydration products and crystal growth, further enhancing the compressive strength of the filling body. Consequently, incorporating an appropriate amount of fly ash into the cement not only reduces cement consumption but also augments the strength of the filling body. However, as the quantity of fly ash increases, the compressive strength of the specimens experiences a decline after reaching its peak. This decline occurs because the advantages provided by the fine aggregates in fly ash cannot fully compensate for its lower reactivity. The test results consistently point to the optimal ratio of cement to fly ash in cementitious materials being 8 : 2.

Figure 4 illustrates the strength fitting curves corresponding to different ratios of cementitious materials. The outcomes from the strength ratio test for filling materials clearly show that, when employing a mass fraction of 70% for the filling slurry, the 28-day strength of specimens with a cement–fly ash ratio of 8 : 2 surpasses that of the other two ratio schemes. Furthermore, considering the strength requirements for filling bodies in the filling mining method, it is crucial that the strength of the filling body exceeds 2.8 MPa at the lower 8 m of the stope, with a cement-to-sand ratio of 1 : 4. In the middle of the stope, the strength of the filling body should be above 1.5 MPa, with a cement-to-sand ratio of 1 : 8. For the upper 2 m of the stope, the strength of the filling body should surpass 2.0 MPa, utilizing a cement-to-sand ratio of 1 : 6. These criteria ensure that the strength requirements of the reserved roadway for the filling body are met.

4. Theoretical Analysis of the Load-Bearing Capacity of Steel Arches

Based on the interaction between U-shaped steel arches and rocks around the roadway, a mechanical model for U-shaped steel arches is established, as illustrated in Figure 5. The steel arches exhibit four constraint reaction forces, rendering them a statically indeterminate structure of the first order. The load on the arch crown is represented as "q_1," and the load at the column leg is denoted as "q_2" ($q_2 = kq_1$). Supports "a" and "d" are simplified as fixed hinge supports.

Through a mechanical analysis of support "d," we derive $\sum M_d = 0$. Therefore, the vertical reaction force at support "d" can be determined by the following Equation [14]:

$$N_2 = \frac{1}{2}\int_0^{\pi} q_1 r \sin\theta d\theta = \frac{1}{2} q_1 r(\cos 0 - \cos\pi) = q_1 r. \quad (1)$$

Given $r = 1.5$ m, the maximum vertical reaction force at support "d" is $1.5q_1$ kN/m. Once the vertical reaction force at support "d" is determined, the vertical reaction force N_1 at support "a" can be calculated.

To compute the horizontal reaction force at the supports of the U-shaped steel arch structure, support "a" on the right side is transformed from a fixed hinge type to a movable hinge type, treating it as a basic statically determinate structure. The corresponding redundant thrust is represented by x_1. Consequently, the horizontal thrust at support "a" is expressed as: $R_2 = x_1$. Additionally, adhering to the deformation compatibility condition, support "a" undergoes no displacement in the direction of thrust x_1. Using the force method principle in structural mechanics to solve internal forces, the typical equation of the force method can be calculated as follows:

$$\left.\begin{aligned} \Delta_1 &= \Delta_{11} + \Delta_{1p} = 0 \\ \Delta_{11} &= \delta_{11} X_1 \end{aligned}\right\}, \quad (2)$$

where X_1 is the horizontal thrust resulting from the change of support "a" is hinge type. Δ_1 is the displacement produced by the simplified basic system of the steel arch structure. Δ_{1p} is the horizontal displacement generated by the independent action of load q_1 on support "a." δ_{11} is the horizontal displacement produced by the independent action of horizontal thrust $X_1 = 1$ on support "a."

Therefore, the horizontal thrust can be calculated by the following equation:

$$x_1 = -\Delta_{1p}/\delta_{11}. \quad (3)$$

The values of Δ_{1p} and Δ_{11} can be determined using the principles of a statically determinate structure. Given that shear force and axial force have a minimal impact on the displacement of the U-shaped steel arch structure, and the primary deformation is bending deformation, we have the following equation:

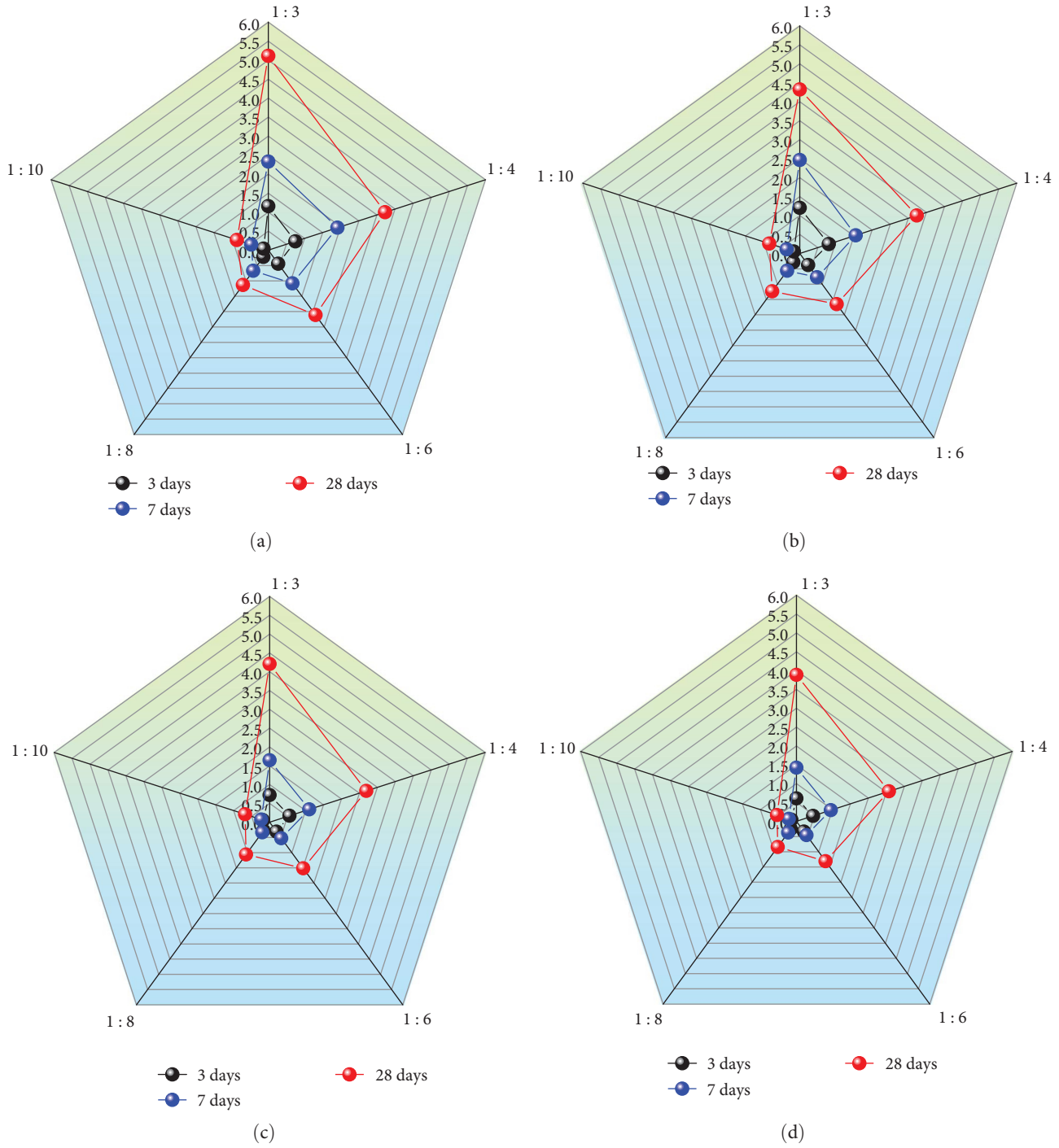

Figure 3: Strength ratio test results: (a) cement, (b) cement : fly ash = 8 : 2, (c) cement : fly ash = 7 : 3, and (d) cement : fly ash = 6 : 4.

$$\left.\begin{aligned}\delta_{11} &= \int \frac{\overline{M_1}^2}{EI}\,ds = \int_{ab} \frac{\overline{M_1}^2}{EI}\,ds + \int_{bc} \frac{\overline{M_1}^2}{EI}\,ds + \int_{cd} \frac{\overline{M_1}^2}{EI}\,ds \\ \Delta_{1p} &= \int \frac{\overline{M_1}M_P}{EI}\,ds = \int_{ab} \frac{\overline{M_1}M_P}{EI}\,ds + \int_{bc} \frac{\overline{M_1}M_P}{EI}\,ds + \int_{cd} \frac{\overline{M_1}M_P}{EI}\,ds\end{aligned}\right\}, \tag{4}$$

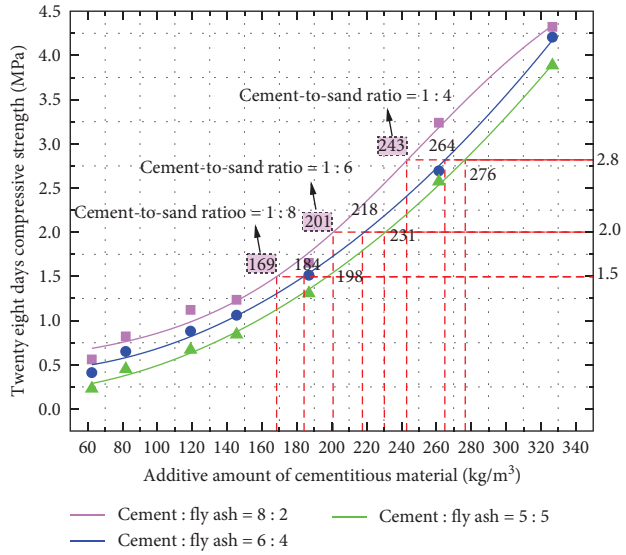

Figure 4: Specimen strength fitting curves.

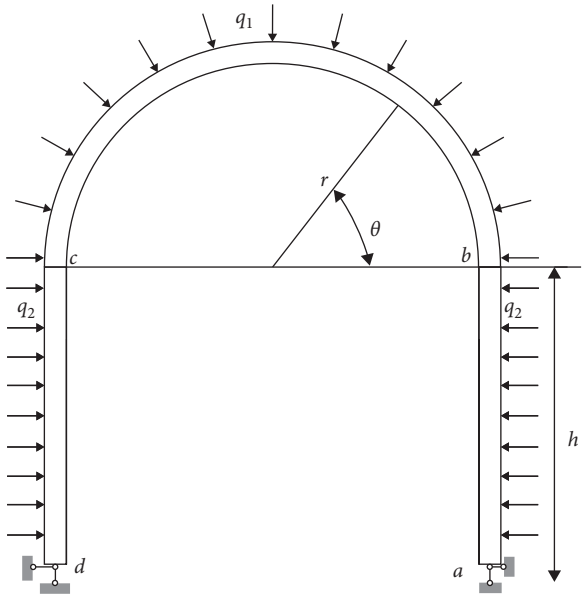

Figure 5: Mechanical model of U-shaped steel.

where E is the elastic modulus of U-shaped steel. M_p is the cross-sectional bending moment of U-shaped steel under the action of load q1 alone. S is the axial length of U-shaped steel. M_1 is the cross-sectional bending moment of U-shaped steel under the action of horizontal thrust $x_1 = 1$ alone. I is the moment of inertia of the section about the neutral axis.

To solve for M_p and $\overline{M_1}$, dividing the U-shaped steel arch structure into segments "ab," "bc," and "cd," we have the following equation:

$$\begin{cases} \overline{M}_1 = x \\ M_p = -0.5kqx^2 \end{cases}. \tag{5}$$

By the equivalence principle, as the "cd" segment is similar to the "ab" segment, we get the following equation:

$$\begin{cases} M_p = -\left(\dfrac{1}{2}l^2 + rl\sin\theta\right)kq \\ \delta_{11} = \dfrac{1}{EI}\left(\dfrac{2}{3}l^3 + \pi r^2 l + \dfrac{\pi}{2}r^3\right) \\ \Delta_{1P} = -\dfrac{kq}{EI}\left(\dfrac{1}{4}l^4 + \dfrac{1}{2}\pi r l^3 + \dfrac{1}{2}\pi r^3 l\right) \end{cases}. \tag{6}$$

By combining the above equations, the horizontal thrust is determined as follows:

$$\begin{cases} F_H = -\dfrac{\Delta_{1P}}{\delta_{11}} = Qkq \\ Q = \dfrac{3l^4 + 6\pi r l^3 + 36r^2 l^2 + 6\pi r^3 l}{8l^3 + 12\pi r l^2 + 48r^2 l + 6\pi r^3} \end{cases}, \tag{7}$$

where l is the height of the U-shaped steel vertical wall, r is the radius of the steel arch structure, and k is the horizontal stress coefficient.

To calculate the load-bearing capacity of the U-shaped steel using force calculations, the axial force at the top is expressed as follows:

$$F_{N2} = (F_H - kql)\sin\theta - qr. \tag{8}$$

The formula for calculating the load-bearing capacity of the U-shaped steel is as follows:

$$F = A\sigma_S, \tag{9}$$

where A is the cross-sectional area of the U-shaped steel and σ_s is the yield limit. Hence, the ultimate load of the U-shaped steel can be given by the following equation:

$$q = \frac{A\sigma_s}{k(Q - l)\sin\theta - r}. \tag{10}$$

According to the specifications for hot-rolled U-shaped steel used in roadway support, Table 2 [15] provides the cross-sectional dimensions and parameters for four common types of U-shaped steel. The ultimate load of the U-shaped steel arch support is directly proportional to the cross-sectional size and yield strength of the U-shaped steel, and inversely proportional to the lateral pressure coefficient. Assuming $r = 1.5$ m, $l = 2.5$ m, and $k = 1$, when substituting the parameters from Table 2 into Equation (9), the ultimate loads for U25, U29, U36, and U40 are calculated as follows: 4.24×105, 4.97×105, 6.60×105, and 7.98×105 N/m, respectively.

If grade 36U-shaped steel is chosen as the primary material for the steel arch support, we can determine the values

Table 2: Cross-sectional parameters of U-shaped steel.

Model	Cross-sectional area (cm^2)	Structural parameter				Tensile strength (MPa)	Yield limit (N/cm^2)
		I_x (cm^4)	I_y (cm^4)	W_y (cm^3)	W_x (cm^3)		
U25	31.54	455.1	506	75.92	81.68	530	33,500
U29	37	612.1	770.7	103	94	530	33,500
U36	45.7	955.5	1,237	148	137	530	36,000
U40	51.02	1,366.9	1,064.1	159.9	141.2	580	39,000

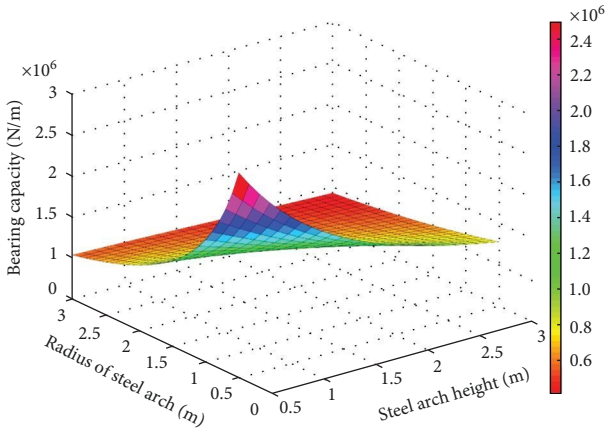

Figure 6: Effect of U-shaped steel vertical wall height and arch radius on the load-bearing capacity of the steel arch support.

for $\sigma_s = 36,000N/cm^2$ and $A = 45.7cm^2$. By conducting a factor analysis using MATLAB based on Equation (10), we establish a relationship that illustrates how the U-shaped steel vertical wall height and the arch support radius influence the load-bearing capacity of the steel arch support, as depicted in Figure 6. The graph indicates an inverse correlation between the load-bearing capacity of the steel arch support and both parameters. Moreover, as these parameters' dimensions gradually increase, the reduction in the load-bearing capacity of the steel arch support progressively slows down. The dimensions of the steel arch support are determined by the size of the reserved roadway, emphasizing the importance of appropriately sizing the roadway to ensure the long-term stability of the reserved roadway.

5. Numerical Simulation Scheme for Reserved Roadway in the Filling Body

5.1. Calibration of Simulation Parameters. To examine the mechanical parameters of the filling body, initial uniaxial compression tests were simulated using FLAC3D. The dimensions of the fitted model matched those of the specimens in the previously mentioned strength tests, encompassing a total of 27,000 model units. A loading rate of 0.3 mm/min was applied to the top and bottom of the model to simulate uniaxial compressive strength tests for the material. Upon comparing the stress–strain curves obtained from numerical simulations with the results of strength tests, a good agreement between simulated and measured values emerged. This alignment provides a valuable reference for exploring the model parameters of filling body materials with different cement-to-sand ratios. For cement-to-sand ratios of 1 : 3, 1 : 4, 1 : 6, and 1 : 8, corresponding model parameters are fitted using a consistent approach. The uniaxial compression models and strength fitting curves for filling body materials are presented in Figure 7, and the obtained numerical model parameters for filling body materials are summarized in Table 3.

5.2. Model Building. To evaluate the deformation of the filling body and determine the optimal cement-to-sand ratio for the load-bearing structure, a numerical analysis model was developed using FLAC^{3D}. The model dimensions, based on the in situ stress conditions and geological information of the +650 m midsection 4001# stope, were set at 155 m × 30 m × 150 m. A centrally reserved horseshoe-shaped roadway with dimensions 4 m × 3 m (height × width) was incorporated. The Mohr–Coulomb constitutive model was applied to the model, with the following boundary conditions: a full displacement constraint on the lower boundary, normal displacement constraints on all sides (left, right, front, and back), and no constraints on the upper boundary. After establishing the model, a Z-direction stress of 15.1 MPa and a lateral pressure coefficient of 1 were applied. The generated mesh was divided into 129,000 elements and 136,353 grids, including a 1 m-thick filling body on the inner wall of the roadway. Beam structural elements were employed to simulate the steel arches and reinforcing bars within the load-bearing structure. The numerical model is illustrated in Figure 8, and the physical and mechanical parameters for each rock layer are provided in Table 4. The analysis concentrated on the mechanical response and the plastic zone range of the roof and floor and steel arches of the reserved roadway in the filling body under the support of the load-bearing structure. The simulation schemes are outlined in Table 5 [16].

The relationships between Young's modulus, shear modulus, and elastic modulus are defined by Equations (11) and (12) [17]:

$$K = \frac{E}{3 \cdot (1 - \nu)}, \tag{11}$$

$$G = \frac{E}{2 \cdot (1 + \nu)}, \tag{12}$$

where E is the elastic modulus and ν is the Poisson's ratio.

5.3. Analysis of Simulation Results. Figure 9(a) depicts the plastic zone distribution around the reserved roadway with a

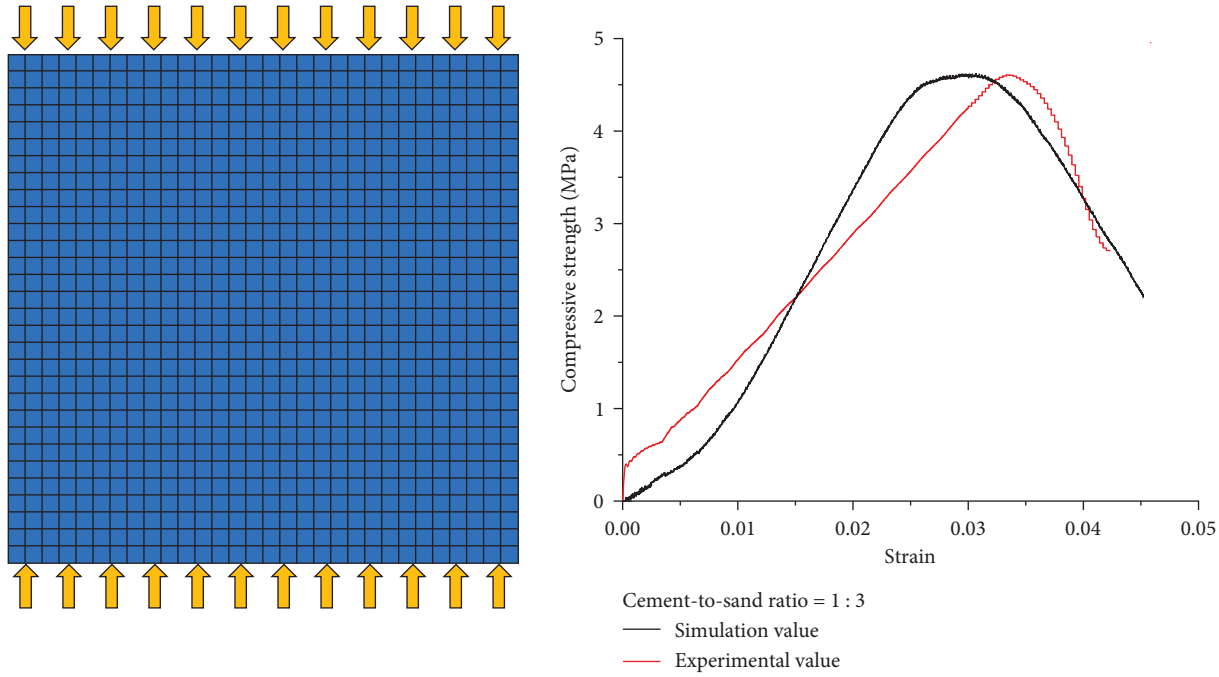

Figure 7: Parameter calibration model and uniaxial curve fitting.

Table 3: Parameters of the uniaxial compressive strength fitting model of filling materials.

Cement-to-sand ratio	Material strength (MPa)	Bulk modulus (MPa)	Shear modulus (MPa)	Cohesion (MPa)	Internal friction angle (degree)	Density (kg/m^3)	Tensile strength (MPa)
1 : 3	4.3	780	560	3.2	40	1.807	0.85
1 : 4	3.2	565	420	3.0	36	1.799	0.78
1 : 6	2.1	482	355	2.4	32	1.797	0.76
1 : 8	1.8	346	290	2.1	31	1.794	0.72

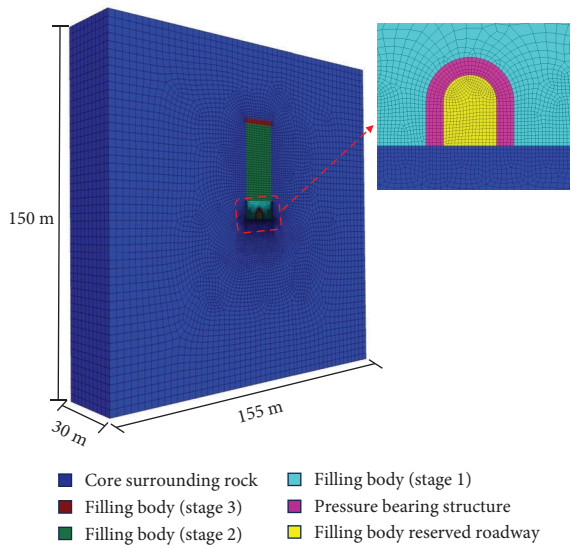

Figure 8: Numerical model.

cement-to-sand ratio of 1 : 3 in the load-bearing structure. The figure reveals plastic zones distributed around the roadway, penetrating to a depth of approximately 1 m in both the roof and floor. The plastic deformation is primarily characterized by shear failure, indicating a tendency for the filling body to experience longitudinal crack formation [18]. Notably, there is a tensile plastic zone at the floor, suggesting tensile stress in the surrounding rock and resulting in some degree of floor heave. The plastic zones on both sidewalls simultaneously reach a depth of 2–3 m, exhibiting both shear and tension failure forms. In this scenario, the sidewalls of the roadway undergo the most severe deformation. In examining the overall distribution of plastic zones, it becomes evident that, after the formation of the reserved roadway, stress redistribution leads to the inevitable occurrence of plastic zones around the roadway. However, under these conditions, the plastic zones are primarily concentrated within a 3 m range around the roadway. The degree of instability and failure of the roadway is relatively limited, and the stability of the surrounding rock can be maintained in the long term through measures such as shaping the roadway or implementing additional support. In Figure 9(b), the plastic zone distribution around the reserved roadway is depicted when the cement-to-sand ratio of the load-bearing structure is 1 : 4. A comparative analysis with the previous scheme indicates a minimal change in the plastic zone range due to the roadway floor being composed of rock. However, there is an expansion of the plastic zone range at the sidewalls and

Table 4: Numerical simulation calculation parameters.

Rock layer name	Bulk (GPa)	Shear (GPa)	Cohesion (MPa)	Friction (degree)	Unit weight (kg/m^3)
Core surrounding rock	6.840	6.550	21.0	40	2,640
Filling body (stage 3)	0.565	0.420	3.0	32	1,799
Filling body (stage 2)	0.482	0.355	2.4	30	1,797
Filling body (stage 1)	0.346	0.295	2.1	29	1,794
Load-bearing structure	Assigned according to fitted parameters for respective cement-to-sand ratios in Table 3.				

Table 5: Numerical simulation schemes.

Numeric simulation scheme	Cement-to-sand ratio of load-bearing structure
Scheme 1	1 : 3
Scheme 2	1 : 4

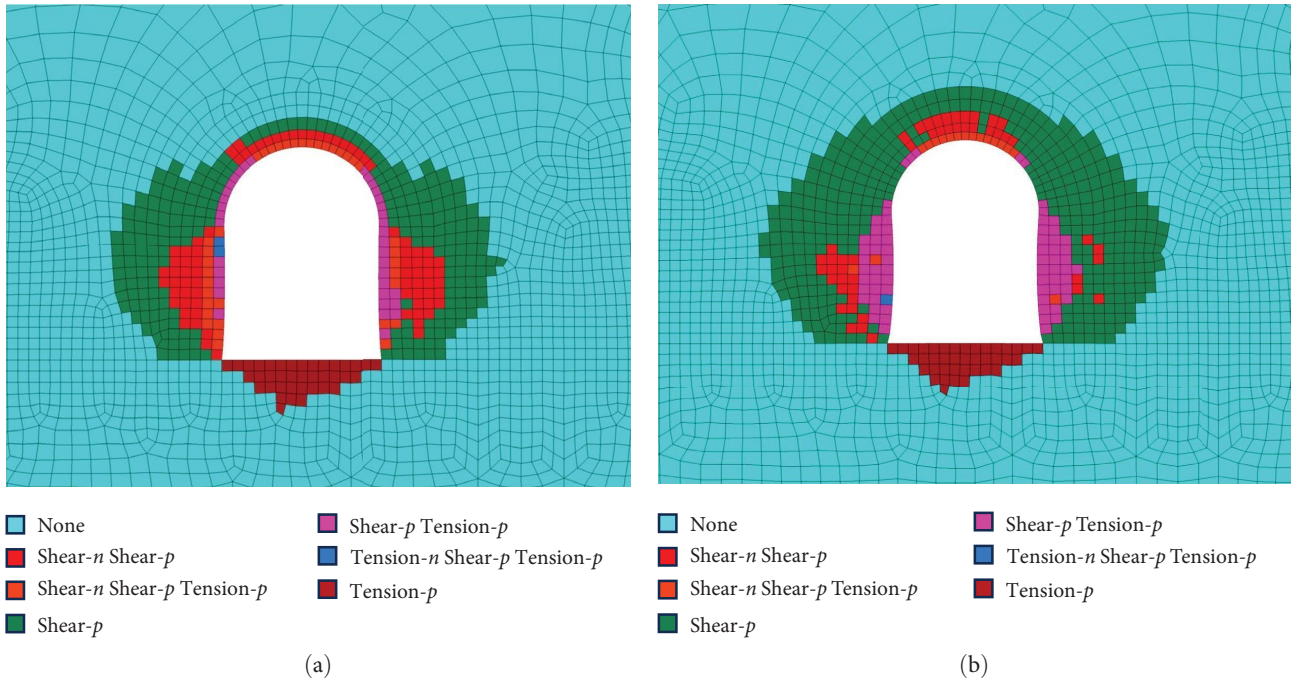

Figure 9: Distribution of plastic zones: (a) load-bearing structure with a cement-to-sand ratio of 1 : 3 and (b) load-bearing structure with a cement-to-sand ratio of 1 : 4.

roof of the roadway. The maximum depth of the plastic zone occurs at the sidewalls, reaching 4 m. Considering that the length of ordinary anchor bolts is generally around 3 m [19] a plastic zone of excessive depth implies challenges in ensuring the formation of a stable load-bearing structure within a certain anchor length.

Figures 10 and 11 present the vertical and horizontal displacement cloud diagrams of the surrounding rock around the reserved roadway under two different cement-to-sand ratios. As can be seen in Figures 10 and 11, with a cement-to-sand ratio of 1 : 3 in the load-bearing structure, the vertical displacement of the roof is 45.1 mm, the floor experiences a vertical displacement of 5.1 mm, the left sidewall exhibits a horizontal displacement of 55.5 mm, and the right sidewall shows a horizontal displacement of 55.6 mm. The maximum roof displacement occurs in the middle, while floor deformation is relatively uniform. The left and right sidewalls deform similarly, moving toward the interior of the roadway. Under the condition of a cement-to-sand ratio of 1 : 4, the vertical displacement of the roof increases to 75.0 mm, the floor vertical displacement is 5.9 mm, the left sidewall undergoes a horizontal displacement of 116.0 mm, and the right sidewall shows a horizontal displacement of 117.0 mm. The deformation pattern is essentially the same as the previous condition, but the vertical displacement has surged by 66.7%. The floor displacement remains relatively small, while the displacements of the left and right sidewalls have increased by 109.0% and 110.4%, respectively. This suggests that elevating the cement-to-sand

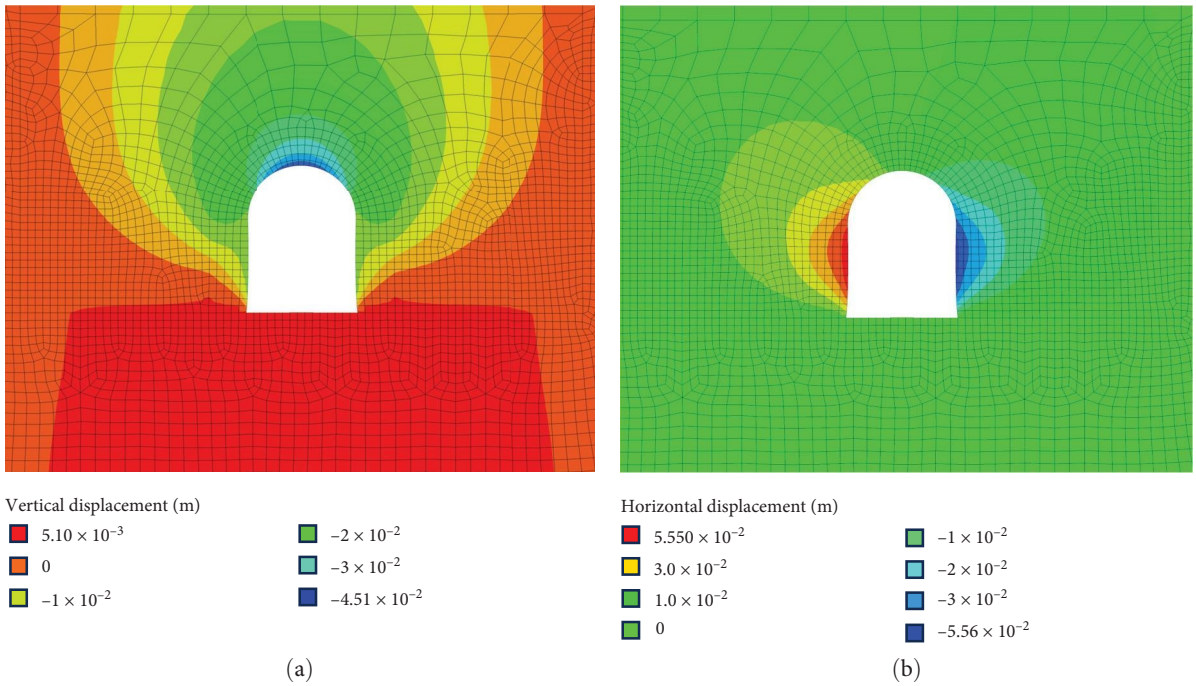

Figure 10: (a, b) Displacement cloud diagram of the surrounding rock of the reserved roadway with a load-bearing structure using a cement-to-sand ratio of 1 : 3.

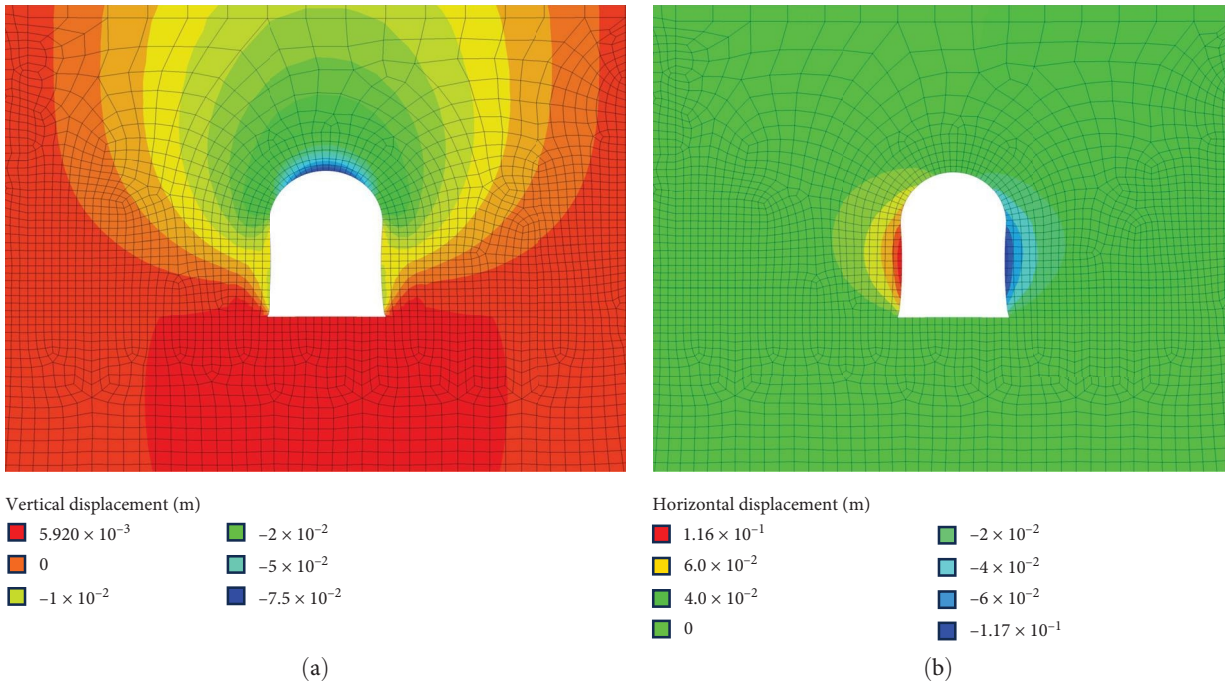

Figure 11: (a, b) Displacement cloud diagram of the surrounding rock of the reserved roadway with a load-bearing structure using a cement-to-sand ratio of 1 : 4.

ratio in the load-bearing structure and implementing a combined support method with steel arches can effectively reduce the extent of damage to the reserved roadway within a filling body.

Figure 12 shows the displacement monitoring curve, by setting monitoring points in the middle of the roof plate and the middle of the left and right gangs, the vertical displacement of the roof plate and the horizontal displacement of the two gangs are monitored. The monitoring results show that the displacement of the roof plate and the left and right gangs are different under different gray sand ratio, and the specific displacement values are consistent with those in Figures 11 and 12, but the common point of the two is that

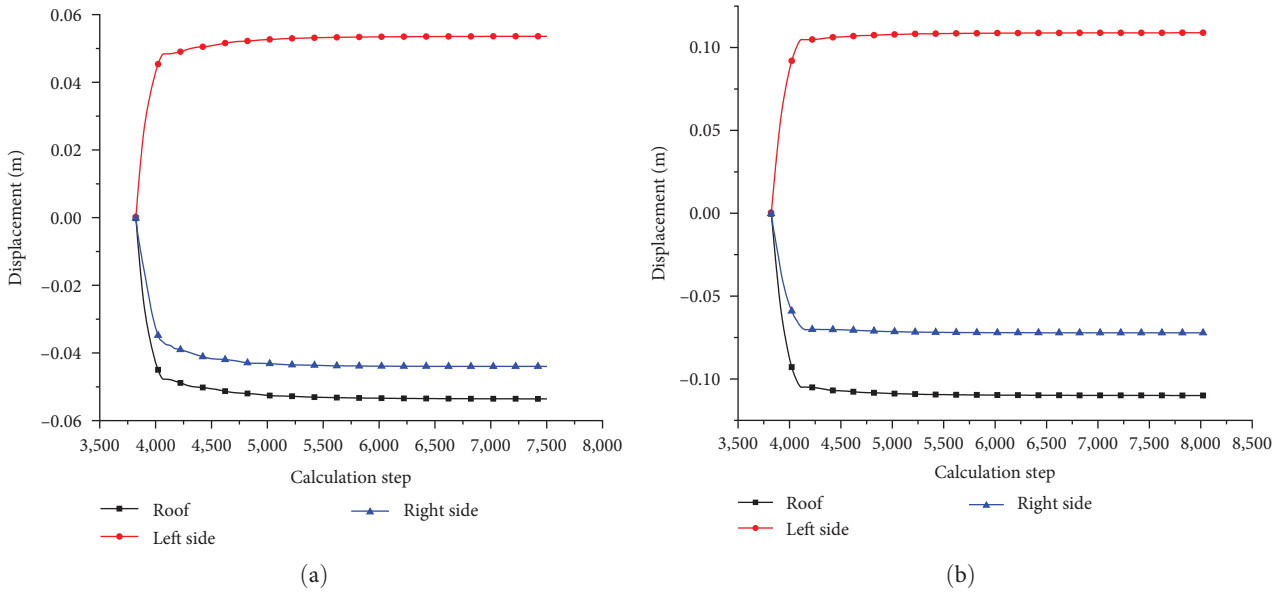

FIGURE 12: Displacement monitoring curve: (a) cement-to-sand ratio of 1 : 3 and (b) cement-to-sand ratio of 1 : 4.

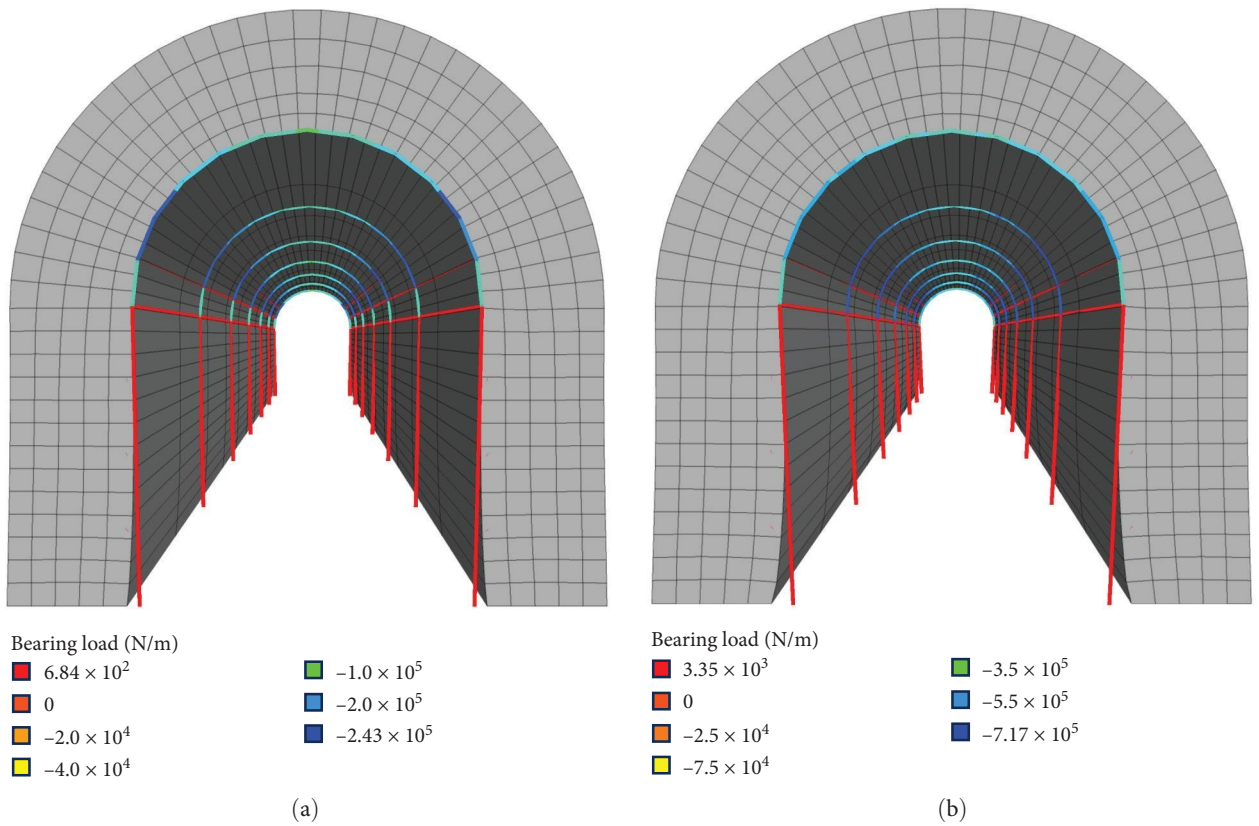

FIGURE 13: Force cloud diagrams of steel arches: (a) load-bearing structure with a cement-to-sand ratio of 1 : 3 and (b) load-bearing structure with a cement-to-sand ratio of 1 : 4.

the deformation of the roadway is in the presimulation period, which indicates that the key period of roadway deformation is during the formation of the roadway.

Figure 13 depicts the force diagrams of the steel arches under two different conditions. In Figure 13, it is evident that when the load-bearing structure adopts a cement-to-sand ratio of 1 : 3, the straight segment of the steel arch experiences tension with a magnitude of 6.84×10^2 N/m, while the arched segment is in compression with a magnitude of 2.43×10^5 N/m. Conversely, when the load-bearing structure adopts a cement-to-sand ratio of 1 : 4, the straight segment of the steel arch is also in tension, with a magnitude of 3.35×10^3 N/m, and the arched

Figure 14: Reserved roadway.

segment is in compression with a magnitude of 7.17×10^5 N/m. For a steel arch with a straight segment length of 2.5 m and an arch radius of 1.5 m, utilizing Equation (10) yields the ultimate bearing capacity of the U36 steel arch as 6.6×10^5 N/m. When the load-bearing structure employs a cement-to-sand ratio of 1 : 3, the load on the steel arch falls within the ultimate bearing capacity range of U36 and U40. Consequently, U36 is selected as the U-shaped steel arch support. On the contrary, with a cement-to-sand ratio of 1 : 4 in the load-bearing structure, the load on the steel arch exceeds the ultimate bearing capacity range of the four types of U-shaped steel, resulting in structural failure and an inability to sustain stability for the roadway.

6. Engineering Practice

Based on the foundational data from stope 4001#, the reserved roadway measures 4 m × 3 m (height × width). The support system employs a filling material with a cement-to-sand ratio of 1 : 3, complemented by U36 steel arches, as depicted in Figure 14. To verify the long-term reliability of the roadway, a cross-point method is employed, positioning displacement monitoring points at the midpoint of the roadway's roof and the midpoints of the left and right sidewalls. Measurements are conducted every 3 days using a tape measure to assess the distances between the roadway's roof and floor, as well as between the two sidewalls. Following the measurements, data are promptly organized and analyzed to comprehend the real-time deformation of the roadway's surrounding rock, as shown in Figure 15. Analysis of the displacement monitoring chart reveals that the deformation of the roadway was relatively gradual in the initial 25 days, with more significant changes occurring between the 25th and 50th days of monitoring. Subsequently, the roadway's deformation essentially stabilized. In conclusion, the monitoring results indicate a maximum roof convergence of 70.1 mm, and the convergence of the left and right sidewalls is 89.6 mm. The deformation of the surrounding rock is within a limited range, providing substantial evidence of the long-term stability of the roadway.

7. Conclusion

(1) The results of the strength ratio test for filling materials establish an ideal cement-to-fly ash ratio for the filling body as 8 : 2. The load-bearing structure for filling adopts a cement-to-sand ratio of 1 : 3. Additionally, specific ratios are employed in different sections of the stope: 1 : 4 for the lower 8 m, 1 : 8 in the middle section, and 1 : 6 in the upper 2 m. These ratios can ensure compliance with necessary strength standards for the reserved roadway.

(2) When the cement-to-sand ratio in the filling body of the load-bearing structure is 1 : 3 and 1 : 4, the deformation trends of the reserved roadway are essentially similar under both conditions. However, a comparative analysis of numerical simulation results reveals that the latter exhibits an expanded plastic zone, with a 66.7% increase in vertical displacement and a 109.0% and 110.4% increase in left and right sidewall displacements, respectively. This suggests that a higher cement-to-sand ratio, forming a higher strength filling body, is advantageous for maintaining the long-term stability of the reserved roadway.

(3) The U-shaped steel vertical wall height and the support arch radius exhibit an inverse relationship with the load-bearing capacity of the steel arch support. As the dimensions of both continue to increase, the decrease in the load-bearing capacity of the steel arch support gradually slows down. When the load-bearing structure adopts a cement-to-sand ratio of 1 : 3, the loads on U36 and U40 steel arches fall within their bearing ranges. However, with a cement-to-sand ratio of 1 : 4, the loads on the steel arches exceed their bearing range. Therefore, it is recommended to use a cement-to-sand ratio of 1 : 3 for the filling slurry to construct the load-bearing structure and U36 steel arches to ensure the long-term serviceability of the steel arches.

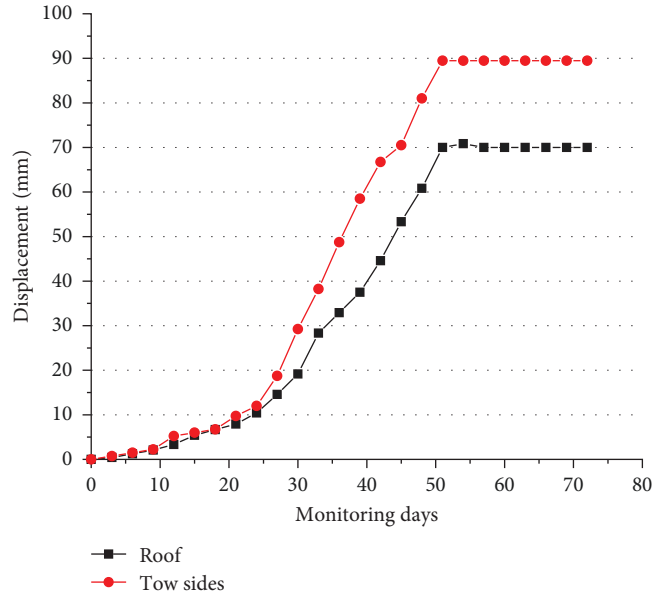

Figure 15: Displacement monitoring curve of surrounding rock at monitoring points.

(4) On-site monitoring indicates that the maximum convergence of the reserved roadway's roof is 89.6 mm, and the convergence of the left and right sidewalls is 70.1 mm. The deformation of the surrounding rock is within a controllable range, ensuring the normal use of the roadway.

Data Availability

All data included in this study are available upon request by contact with the corresponding author.

Conflicts of Interest

The authors declare that they have no conflicts of interest.

Acknowledgments

This work was supported by the National Key R&D Program of China (2022YFC2904002, 2022YFC2904003).

References

[1] S. Wu, X. Yang, and L. Guo, "Thinking and prospect of overall planning for deep metal mine in high stress environment," *Journal of China Coal Society*, vol. 44, no. 5, pp. 1432–1436, 2019.

[2] N. Ma, H. Ma, Y. Wang, and K. Lyu, "Support principle and flexible cable support technology of deep large deformation roadway," *Safety Engineering*, vol. 40, no. 5, pp. 957–964, 2023.

[3] W. Peng, H. Zhuq, and Q. Wang, "Stress distribution law of surrounding rock bearing structure of broken surrounding rock roadway," *Journal of Central South University(Science and Technology)*, vol. 54, no. 6, pp. 2447–2458, 2023.

[4] Y. Yu, D. Chen, X. Zhao, X. Wang, L. Zhang, and S. Zhu, "Stabilization mechanism and safety control strategy of the deep roadway with complex stress," *Advances in Civil Engineering*, vol. 2020, Article ID 8829651, 18 pages, 2020.

[5] G. Xue, E. Yilmaz, and Y. Wang, "Progress and prospects of mining with backfill in metal mines in China," *International Journal of Minerals, Metallurgy and Materials*, vol. 30, no. 8, pp. 1455–1473, 2023.

[6] J. Chen F. Liu, X. Zhang, J. Wang, H. Jiao, and J. Yu, "Review on the art of roof contacting in cemented waste backfill technology in a metal mine," *Minerals*, vol. 12, no. 6, Article ID 721, 2022.

[7] Q. Chang, Y. Sun, Q. Leng, Z. Liu, H. Zhou, and Y. Sun, "Stability analysis of paste filling roof by cut and fill mining," *Sustainability*, vol. 13, no. 19, Article ID 10899, 2021.

[8] M. He and Q. Wang, "Rock dynamics in deep mining," *International Journal of Mining Science and Technology*, vol. 33, no. 9, pp. 1065–1082, 2023.

[9] J. Ke, "Research on excavation roadway support technology in the filling body in stopes," *Gold*, vol. 43, no. 10, pp. 38–43, 2022.

[10] F. Luo, "Stability analysis of reserved tunnels in fill body under dynamic disturbance," *Gold*, vol. 44, no. 6, pp. 4–10, 2023.

[11] H. Deng, L. Luo, and S. Li, "Study on mechanical response of backfill under dynamic disturbance," *Journal of Safety Science and Technology*, vol. 12, no. 2, pp. 62–67, 2016.

[12] Z. Zhang, J. Bai, and X. Wang, "Review and development of surrounding rock control technology for gob-side entry retaining in China," *Journal of China Coal Society*, vol. 48, no. 11, pp. 3979–4000, 2023.

[13] Z. Ruan, A. Wuh, and H. Fu, "Influence mechanism of straw fiber on uniaxial compressive strength cemented paste backfill body of sulfur-bearing tailings," *Journal of Central South University (Science and Technology)*, vol. 54, no. 3, pp. 837–848, 2023.

[14] A. Carpinteri, *Structural Mechanics*, Taylor and Francis, 2017.

[15] H. Wang, D. Deng, and Y. Jiang, "Investigation on the ultimate load bearing capacity of U-shaped steel arch support in coal bursting mine," *Journal of Mining Science and Technology*, vol. 6, no. 2, pp. 176–187.

[16] K. Li, W. Yu, Y. Xu, Z. Zhou, M. Xu, and W. Liang, "Analysis on the influence degree of deformation control factors of deep-buried roadway's fractured surrounding rock using orthogonal design," *Advances in Civil Engineering*, vol. 2021, Article ID 9981539, 11 pages, 2021.

[17] H. Zhu, W. Peng, and S. Zou, "Study on treatment of chamber floor heave in broken surrounding rock of deep mine," *Coal Technology*, vol. 40, no. 5, pp. 4–8, 2021.

[18] W. Wang, G. Guo, and Y. Zhu, "Malignant development process of plastic zone and control technology of high stress and soft rock roadway," *Journal of China Coal Society*, vol. 40, no. 12, pp. 2747–2754, 2015.

[19] H. Kang, T. Jiang, and F. Gao, "Design for pretensioned rock bolting parameters," *Journal of China Coal Society*, vol. 7, pp. 721–726, 2008.